An assessment of tunneling-multiphoton dichotomy in atomic photo-ionization: Keldysh parameter γ versus scaled frequency Ω

Turker Topcu and Francis Robicheaux

Department of Physics, Auburn University, Alabama 36849-5311, USA

(Dated: May 17, 2012)

It is commonly accepted in strong-laser physics community that dynamical regime of atomic ionization is described by the Keldysh parameter, γ. Two distinct cases where $\gamma > 1$ and $\gamma < 1$ are associated with ionization mechanisms that are predominantly in the tunneling and in multi-photon regimes, respectively. We report on our fully three-dimensional *ab initio* quantum simulations of ionization of hydrogen atoms in laser fields described in terms of the Keldysh parameter by solving the corresponding time-dependent Schrödinger equation. We find that the meaning of the Keldysh parameter changes when the laser frequency ω is changed, and demonstrate that it is useful in determining the dynamical ionization regime only when coupled with the scaled laser frequency, Ω, when a large range of laser frequencies and peak intensities are considered. The scaled frequency Ω relates the laser frequency ω to the classical Kepler frequency ω_K of the bound electron, and together with the Keldysh parameter, the couple (γ, Ω) refers to a more realistic picture of the dynamical ionization regime. We then refer to final momentum distributions of the ionized electrons at several interesting points on the (γ, Ω) landscape, in order to infer whether tunneling or multi-photon mechanism is dominant in these regions.

I. INTRODUCTION

It has been ubiquitous in strong-laser physics that the dynamical regime of atomic ionization, whether it be field ionization or ionization through absorption of photons, is associated with the Keldysh parameter, γ [1, 2]. In strong lasers, the Coulomb field experienced by the atomic electron is depressed by the strong laser field. Depending on the peak field strength of the laser field, this depression can be substantial so as to result in a potential barrier oscillating at the laser frequency. Quantum mechanically, there is non-vanishing probability that the electron can tunnel through this barrier and escape into the continuum. The likelihood of ionization in this manner is quantified by the conditions in which the Keldysh parameter is less than unity, $\gamma < 1$. This is commonly referred to as the quasi-static limit, in which the depressed Coulomb barrier is essentially static as seen by the electron. When $\gamma > 1$, the atom ionizes by absorption of a number of photons and the electron escapes through either direct or indirect paths of ionization. However, $\gamma > 1$ does not necessarily mean that there is no tunneling contribution to the ionization, it is meant to imply when the tunnel ionization is most likely.

Keldysh theory is strictly a theory of tunneling [1–3]. In Keldysh-like strong field theories, the classical action is always complex regardless of γ, therefore its description is always contained within the tunneling picture. In other words, ionization through a classically allowed path does not occur in Keldysh-like theories. Therefore, the statement that $\gamma > 1$ corresponds to multi-photon ionization is not a statement made directly by the Keldysh theory, but rather is a deduction which incorporates conservation of energy with the prediction that $\gamma < 1$ refers to ionization dynamics governed predominantly by tun-

neling. It predicts the ionization rates when tunneling is most likely, and when there is ionization with $\gamma > 1$, we deduce that it must have followed an ionization path that is not tunneling, i.e. one characterized by absorption of photons. This is the step that incorporates the conservation of energy into the argument which ultimately decides that the ionization happens through photon absorption.

Several shortcomings of the Keldysh-like theories is evident from the approximations made to the S-matrix elements to allow for closed analytical expressions. For example, theories such as SFA (strong field approximation) involves no dynamics within the potential barrier, are not gauge invariant, and the result usually depends on the choice of the origin [4–7]. Less obvious shortcomings of the applicability of the Keldysh parameter as an index for assessing ionization regimes have also been demonstrated and it has been shown to be unsuitable to describe laser-induced ionization when a wide range of frequencies are considered. Even when $\gamma < 1$, the laser frequency can be so high as to allow for ultra-intense fields while keeping the Keldysh parameter small. In such instances, $\gamma \to 0$ limit converges to the fully relativistic conditions, where the ponderomotive energy $U_p = F^2/4\omega^2$ becomes comparable to the rest energy of the electron [8]. This invalidates the $\gamma \to 0$ limit as the static field limit in which ionization simply occurs through field ionization.

The reasoning behind the Keldysh parameter is the following: In the standard Keldysh theory, the tunneling length is $L \sim I_p/F$, where I_p and F are the ionization potential and the peak electric field strength. The velocity in the classically forbidden region, where the combined Coulomb and the electric field potential is larger than the total energy of the electron, can be obtained using the WKB approximation to be roughly $v \sim \sqrt{2I_p}/2$. Then the time it takes for the electron to

tunnel through the depressed Coulomb potential is essentially $\tau \sim L/v = \sqrt{2I_p}/F$. The ratio of this tunneling time to the laser period is a measure of how fast the barrier oscillates compared to the time it takes for the electron to tunnel ionize, i.e. $\omega\tau$ where ω is the laser frequency. This ratio is $\gamma = \omega\sqrt{2I_p}/F$ and referred to as the Keldysh parameter. It tells how static the oscillating potential is as seen by the bound electron. The barrier is effectively static with regard to the time it takes the electron to tunnel ionize when $\gamma < 1$ (or $T > \tau$), and oscillating if $\gamma > 1$ (or $T < \tau$). Trouble with exploiting the Keldysh parameter for a wide range of frequencies is immediately evident from this definition. Note that γ is linearly proportional to ω whereas it is inversely proportional to F. Therefore for a fixed laser wavelength, one can vary the laser intensity in ways such that any value for the Keldysh parameter can be attained. Conversely, fixing the field intensity, one can vary the wavelength to get any γ desired. This point of view does not respect conservation of energy and relevant time scales other than the laser period, such as the classical orbital period of the electron, and incorrect deductions can be drawn for ionization dynamics for certain sets of parameters. For example, assuming a fixed $\gamma \ll 1$, we can keep choosing smaller and and smaller intensities for a laser pulse, which may push the photon energy well into the X-ray region. However, it would be unreasonable to expect that ionization by such a laser pulse would happen through tunneling.

Experiments such as the ones in Refs. [9, 10] have suggested that the ratio of the laser frequency ω to the classical orbital frequency ω_K of the bound electron, i.e. ω/ω_K, is more important in deducing the relevant physical mechanisms than the laser frequency ω alone. This ratio is termed the scaled frequency and is given by $\Omega = \omega n^3$ for atoms. The reasoning behind this is evident if one considers that absorption of a photon by an atomic electron is most likely when the electron is near the nucleus. This happens once in every orbital period, $2\pi/\omega_K = 1/n^3$. When $\Omega < 1$, effect of the field is similar to that of a static field and the field strength required for ionization scales like $F \sim 1/9n^4$. When $\Omega \to 1$, multiphoton transitions occur to higher n-states, which are more easily ionized. In this regime, the ionization rate scales $\sim F^{2N}$, where N is the number of photons absorbed during ionization. $\Omega > n/2$ or $\omega > 1/2n^2$ is the single-photon ionization limit after which photoionization occurs through absorption of a single photon of higher frequency, and the field strength needed for ionization drops below $1/9n^4$.

For our purposes, it is more natural to express the Keldysh parameter in terms of the scaled parameters, Ω and F, rather than ω and F. Scaling the field strength by $1/n^4$ and noting that $\omega = \Omega/n^3$, we can rewrite the Keldysh parameter in terms of the scaled frequency and the electric field strength:

$$\gamma = \frac{\omega\sqrt{2I_p}}{F} \to \frac{(\Omega/n^3)\sqrt{1/n^2}}{F/n^4} = \frac{\Omega}{F} \qquad (1)$$

where the scaled frequency is $\Omega = \omega n^3 \sim \omega/\omega_K$, and the Keldysh parameter no more bears any dependence on n.

We perform two sets of calculations for ionization of a Hydrogen atom out of $1s$, $2s$, $8s$ and $16s$ states in laser fields: one for the ionization rate and one for the ionization probability for a large set of (γ, Ω) pairs. We map out a landscape in (γ, Ω) space, which shows regions bearing characteristics that can be attributed to either tunneling or multiphoton features. Then calculating final momentum distributions of the ionized electrons at a select few points on our (γ, Ω) map for large and small γ, we try to determine whether field or multiphoton ionization is dominant in these regions.

II. NUMERICAL SIMULATIONS

In our rate calculations, we use a continuous wave (cw) laser for the rate calculations and a laser pulse with finite a width of 160 Rydberg periods at FWHM for the probability calculations. All of our simulations are based on *ab initio* solutions of the three-dimensional time-dependent Schrödinger equation in the length gauge. We represent the total wave function on an (l, r) grid with a square-root mesh in the r-direction. We use the lowest order split operator technique for the time propagation of the Schrödinger equation, where each split piece is propagated using an $\mathcal{O}(\delta t^3)$ implicit scheme. This is an exactly unitary propagator, and enables us to use larger time steps during the time propagation compared to those needed for an explicit scheme. We use a mask function starting from $2/3$ of the box from the origin to remove the ionized part of the wave function in order to avert spurious reflections from the box edge. A detailed account of the $\mathcal{O}(\delta t^3)$ implicit method and the split operator technique employed in this work can be seen in Ref. [11]. Below we only discuss the differences in our simulations for the ionization rates and probabilities. The number of the (γ, Ω) pairs we include in our simulations is 12,000, which is achieved by massive parallelization over 12,000 (γ, Ω) pairs. We use atomic units throughout this paper unless we explicitly indicate otherwise.

We employ a time-dependent approach reminiscent of the time-dependent perturbation theory for our rate calculations. We split the total hamiltonian of the system into two pieces, such that $H(r, l, t) = H_A(r, l) + H_L(r, t) - E_0$, where H_A is the atomic hamiltonian and H_L is the hamiltonian describing the interaction of the atom with the laser field in the length gauge:

$$H_A(r, l) = -\frac{1}{2}\frac{d^2}{dr^2} - \frac{1}{r} + \frac{l(l+1)}{2r^2} \qquad (2)$$

$$H_L(r, t) = F(t)z\cos(\omega t) \qquad (3)$$

We subtract energy of the initial state E_0 from the hamiltonian, and express the total wave function as a superposition of the initial eigenstate of H_A, and the time-dependent correction, $\psi(r,l,t) = \psi_0(r,l) + \psi_1(r,l,t)$, to write the time-dependent Schrödinger equation as

$$\left[i\frac{\partial}{\partial t} - H(r,l,t) \right] \psi_1(r,l,t) = H_L \psi_0 \qquad (4)$$

with $H_L(r,t)\psi_0(r,l)$ acting as a source term. Given that $\psi(t) = \psi_0 + \psi_1(t)$, and that ψ_0 is an eigenstate of H_A, Eq. 4 is exact and allows for atomic processes of all orders, such as absorption of multiple photons, as well as single-photon processes and tunneling. The wave function $\psi_1(t)$ is zero everywhere before the laser pulse is turned on, and it is analogous to the first order correction to the initial wave function in the time-dependent perturbation theory, except that it now encodes all the higher order contributions. As the pulse is turned on, amplitude pours out of the initial state ψ_0 into ψ_1 at a rate defined by the instantaneous field strength. After the flat top of the laser envelope is reached we wait for the time-dependent ionization flux $J_R(t)$ to settle down at a steady state, which we then term as the ionization rate. We evaluate the time-dependent flux $J_R(t)$ through a spherical surface far away from the origin,

$$J_R(t) = \sum_l \psi_{l,j}^* \left(\frac{\psi_{l,j+1} - \psi_{l,j-1}}{r_{j+1} - r_{j-1}} \right). \qquad (5)$$

Here R is the radius of the spherical surface through which we evaluate the flux. It is also the distance from the origin beyond which the mask function becomes effective. The time-dependent envelope for the laser pulse turn on is

$$F(t) = \begin{cases} F_0 \exp[-(t/\Delta t)^4] & , t < 0 \\ F_0 & , t \geq 0 \end{cases} \qquad (6)$$

where we take Δt to be 10 laser periods. We found that faster turn on times result in ringing in the ionization flux, which starts to increase the propagation time required for the ionization rate to settle down at a steady state. On the other hand, slower turn on rates also result in higher computational overhead since it prolongs the total propagation time of Eq. 4.

For our second set of simulations, we solve the time-dependent Schrödinger equation to calculate ionization probabilities:

$$\left[i\frac{\partial}{\partial t} - H(r,l,t) \right] \psi(r,l,t) = 0 \qquad (7)$$

with the initial wave function being a bound state of Hydrogen with $l = 0$, i.e. $1s$, $4s$, and $8s$. Note that the operator acting onto $\psi(r,l,t)$ on the left hand side is the same operator as in Eq. 4. We evaluate the ionization probability as the norm of the wave function which is absorbed by the mask starting from $2/3$ of the radial box. The initial wave function is normalized to unity.

In all of our calculations, we regularly perform convergence checks on several relevant numerical parameters, such as number of grid points and angular momenta as well as the size of the time steps taken during the propagation of Eqns. 4 and 7. Since there are two inherent time scales involved in the problem, i.e. the Rydberg period τ_R of the electron and the laser period $2\pi/\omega$, we pay special attention to our choice of the time step to make sure that we have enough points in time within the smallest time scale for a given (γ, Ω) pair. Specifically, our choice of time step is

$$\delta t = \begin{cases} c_1(2\pi/\omega) & , 2\pi/\omega < \tau_R \\ c_2\, \tau_R & , 2\pi/\omega \geq \tau_R \end{cases} \qquad (8)$$

where the factors $c_1 = 1/800$ and $c_2 = 1/200$ gave us converged results for all (γ, Ω) pairs we considered. In choosing the number of grid points N for a box of size R using the square-root mesh in the r-direction, we make sure that $\max(k\delta r) < 1$ everywhere inside the box. Specifically, we monitor $k\delta r$ where the mask function starts to weigh in (r_{mask}), and at the box edge. Given that we use a square-root mesh where $r_j = j^2 R/N^2$ ($0 \leq j < N$) and a mask function starting from $1/3$ of the way from the box edge, for the maximum Ω we consider, we deduce that

$$\max(k\delta r_M) = \frac{4R}{N} \left(\frac{\Omega_{max}}{3n^3} \right)^{1/2}$$

$$\max(k\delta r_R) = \frac{2R}{N} \left[2\Omega_{max}/n^3 \right]^{1/2}$$

where $k = (2E)^{1/2}$. The grid spacing δr_M is at the starting position of the mask function, and δr_R is the largest grid spacing at the end of the radial box. When we take E_{max} to be the largest photon frequency in our rate and probability calculations, we found that our results for the rate calculations were reasonably converged when $\max(k\delta r_R) \sim 0.76$ for $n = 1$, ~ 0.36 for $n = 4$, and ~ 0.32 for $n = 8$. In the probability calculations, we had $\max(k\delta r_R)$ values smaller than these by a factor of 4 because we only go up to $\Omega = 4$ in our probability calculations, whereas $\Omega = 64$ is the largest scaled frequency in the rate calculations. The values for $\max(k\delta M)$ are slightly lower than these since the grid spacing is smaller at smaller r.

III. RESULTS AND DISCUSSION

A. Ionization Rate

Fig. 1 shows the steady flux of ionizing electrons, which we interpret as ionization rate Γ, from initial states of $1s$, $4s$, $8s$, and $16s$ for Hydrogen atom. The scaled frequency Ω ranges from 0.05 to 64 and is plotted in $\log_2$ scale to display such a wide range of frequencies in a single plot. The vertical axes are the Keldysh parameter γ, which

ranges from 0.1 a.u. to 2 a.u. and are plotted in linear scale. The ionization rates Γ are plotted in $\log_{10}$ scale and the contours decrease from yellow (bright) to blue (darker). For a fixed Ω, the ionization rate ultimately increases as γ decreases because γ is inversely proportional to the field strength at fixed Ω. This is naturally expected since regardless of the driving frequency, there is a high enough field intensity which will result in ionization. For the lowest Ω value in Fig. 1, F varies from 1.3×10^7 to 6.4×10^7 V/cm as γ varies from 2 to 0.1, which correspond to intensities of $\sim 9 \times 10^{15}$ and $\sim 4 \times 10^{14}$ W/cm^2. On the other hand, for the highest Ω, the electric field strength varies between 32 and 640 a.u. as γ varies from top to bottom, which correspond to ultra high intensities of $\sim \times 10^{18}$ and $\sim 2 \times 10^{19}$ W/cm^2, respectively. These four intensities correspond to the four limiting cases situated at the four corners of each (Ω, γ) map.

Photon energies in eV corresponding to the Ω values are also indicated on the upper horizontal axis for reference. Note that even the minimum of these intensities is fairly large for a Hydrogen atom. This stems from our choice for the ranges of Ω and γ in Fig. 1, which is motivated by the desire to straddle $\gamma = 1$ in an Ω range that runs from $\Omega \ll 1$ to $\Omega \gg 1$. In reality, for most of the (Ω, γ) pairs in Fig. 1, ionization would very quickly saturate for a laser pulse that spans even a few orbital periods of the electron. The important thing to remember here is that Fig. 1 is a map for the ionization *rate*.

The fact that ionization would saturate immediately for most of the maps in Fig. 1 is evident from the green contours. The regions enclosed by these contours are where the ionization rates are larger than the classical frequency $1/(2\pi n^3)$, i.e. where the ionization happens in less than a classical orbital period of the electron. In this case, rate as a concept ceases to be meaningful, and any structure within these interior regions of the green curves tell little about the dynamics leading to ionization since the ionization probability will very quickly saturate.

Inarguably the most striking feature in these maps is the *ridge* structure, which is most prominent and clear in the (Ω, γ) map for $1s$. Although they don't appear to be vertically straight due to the $\log_2$ scaling of the Ω axis, each of these ridges are at a fixed Ω value. Also note that there are more than one ridge in these figures. These correspond to the Ω that are the 1-, 2-, $\cdots$, N-photon ionization thresholds, and can be written as $\Omega_N = \omega_N/\omega_K = n/(2N)$. Here ω_N is the laser frequency needed for N-photon ionization. The most prominent ridges are those for $N = 1$ (single-photon ionization), and the smaller subsequent ridges to its left are the ones that correspond to multi-photon ionization with the absorption of 2 or more photons. In this multi-photon region $\Omega < n/2$, and the ridges gradually disappear as $\Omega \to 0$, when the oscillation of the laser field becomes much slower than the classical orbital motion of the electron. In this case, the depressed Coulomb potential is essentially static with regard to the tunneling time of the electron, and ionization mainly occurs through field

ionization for all γ. For such values of Ω with $\gamma > 0.5$, ionization rate drops drastically even well before $\gamma = 1$ is reached.

To the right side of the single-photon ionization ridge, ionization rate drops with increasing photon energy for a fixed γ. In this region of high scaled frequency, ionization is suppressed, and higher and higher photon intensities are required to maintain given rate of ionization if Ω is increased. This suppression of ionization has been observed in experiments for microwave ionization out of high Rydberg states [12, 13]. It can be understood considering that the higher the Ω, the smaller fraction of its orbit the electron will spend near the nucleus, where it is most likely to absorb a photon, thus rendering the electron less able to absorb photons. An alternative way to think about this that the bigger Ω means a bigger energy change when a photon is absorbed. The bigger the energy change in the final wavefunction, the smaller the region of space is where the initial and final wavefunctions have similar momenta $k(r)$. Absorption of a single photon is sufficient for ionization in this region. For instance, at 1.7 keV for $1s$, γ needs to be less than 0.3 for $\Omega > 16$ in order to maintain the same ionization rate for $\Omega \sim 4$. Clearly, we cannot say that ionization at these high Ω occurs through field ionization any more, and the statement that $\gamma < 1$ refers to tunneling is misleading.

On top of the (γ, Ω) maps in Fig. 1, we plot lines along which the peak electric field strength is a constant. The solid, dashed, and dotted lines correspond to $F = 0.05$, 0.1, and 0.5 a.u., and such slices in Fig. 1 can be taken to extract the energy spectrum at a fixed intensity. In the left column of Fig. 2, we take the spectroscopic point of view for photoionization, and depict ionization rates as a function of Ω for three individual field strengths for initial states of $1s$, $4s$, and $8s$ corresponding to the constant F slices seen in the (γ, Ω) maps of Fig. 1. The classical frequency $1/2\pi n^3$ is indicated for each initial state by the horizontal dashed line (green contours in 1). Portions of the curves that lie above this line correspond to cases in which ionization occurs in less than a classical period, and should not be interpreted as ionization rates. The rates are plotted in $\log_{10}$ scale as in Fig. 1, although the Ω axis is now in linear scale. $F = 0.5$, 0.1, and 0.05 a.u. from top to bottom in each panel on the left, and as expected, the overall magnitudes of the ionization rates drop as the peak field strength decreases. This is due to the well known power law dependence of the rate on the intensity for an N-photon absorption process, $\Gamma \sim F^{2N}$ (see [2] and references therein). Although the intensities seen in this column is somewhat high for hydrogen, ionization with two distinct characteristics can be easily identified in the low and and the high frequency regions. In the low Ω part of the spectra, the rates drop much faster with the decreasing intensity when compared with the higher frequency region. This is a manifestation of the Ω independent decay in the tunneling regime, where the decay rate decreases exponentially with the inverse of the field strength, i.e. $\Gamma \sim \exp[-2(2I_p)^{3/2}/(3F)]$ in the

static field limit [2]. On the other hand, before the sharp drop in the rate is reached for small Ω, there is a relatively flat region which shows little dependence on the scaled frequency. This Ω-independent part of the spectra is the tunneling region, in which Γ obeys the exponential decay of the ionization rate.

In contrast, the rate displays structures in the higher frequency region, which correspond to the multiphoton resonance structure of the atom. The Rydberg-sequence structure of the multiphoton peaks mark the indirect paths of excitation followed by multiphoton ionization from an excited state. The positions of these peaks experience AC stark shifts from the laser field, and the position of Ω_1 is closest to $n/2$ for the lowest F. This regime persists until the higher Ω region is reached beyond the single-photon ionization limits $\Omega_1 = 0.5$, 2, and 4 for $n = 1$, 4, and 8. The ionization in this region is mainly described by the Fermi's golden rule and the drop in the rate in this case is due to the power law dependence of Γ on the intensity. An important caveat here is that when we refer to multi-photon ionization, we are not making any distinction between direct and indirect paths of ionization through absorption of many photons.

After the multiphoton structure is diminished beyond the single-photon ionization limit, the ionization is again suppressed, as discussed in [12, 13] for Rydberg atoms in microwaves. This suppression is argued to be a quantum mechanical interference effect, and the field needed for ionization tends to be n-independent. Such a trend can also be seen in the left column in Fig. 2, as the region of high Ω is penetrated beyond Ω_1, the order of magnitude rates qualitatively start agreeing for $n = 4$ and 8.

Assuming the strong-field physics point of view, right hand column of Fig. 2 shows the ionization rates out of the same set of initial states of Hydrogen as a function of the scaled electric field strength Fn^4 for various scaled frequencies. These plots correspond to constant vertical Ω slices in Fig. 1, and they are plotted as a function of the field strength Ω/γ rather than the Keldysh parameter. Notice that for the low values of Ω, there is a flat plateau region after $Fn^4 \gtrsim 0.2$, suggesting that ionization rate drops like $1/n^4$ in this region. This is a signature of the static field ionization regime, meaning that the distinction between ionization rates for different Ω disappears in this region. This is especially so for the higher n. The higher the principal quantum number the more independent is the rate from the scaled frequency Ω. The rate at the single-photon ionization limit is only plotted for $1s$ ($\Omega_1 = 0.5$), and higher order photo-ionization peaks appear at the low field end of the $4s$ and the $8s$ plots. For the lowest fields in these figures, Γ for the higher frequencies drop much faster than the lower ones, which is a behaviour more pronounced for the higher n-states. This can again be understood considering that at low Ω, the rates decay according to the exponential law $\Gamma \sim \exp[-2(2I_p)^{3/2}/(3F)]$. Recalling that the field scales like $\sim 1/n^4$, and the ionization potential like $\sim 1/n^2$, the exponent would increase as $\sim n$

when plotted against the field strength, resulting in the diminishing of the ionization rate.

B. Ionization Probability

Fig. 3 shows the ionization probabilities out of $1s$, $4s$, and $8s$ states for Hydrogen in (γ, Ω)-space, where γ varies between 0 and 64, and Ω between 0.025 and 4. In contrast with the rate calculations, probability calculations are performed using a finite duration laser pulse with a width of 160 Rydberg periods at FWHM. This corresponds to a pulse width of 80 fs for $1s$, ~ 1.5 ps for $4s$, and ~ 12 ps for the $8s$ state. The contours are color coded such that the bright yellow regions indicate saturation of the ionization probability, i.e. complete ionization. An important difference to keep in mind when relating Fig. 3 to Fig. 1 is that γ- and Ω-axes span different ranges. Also the Ω-axis is in linear scale in Fig. 3, which is why the curved ridges seen in Fig. 1 is replaced by the straight peaks occuring at fixed values of Ω in Fig. 3. Regions with $\gamma < 2$ in Fig. 3 are essentially all saturated for the pulse width used for these simulations such that we needed to go up in γ as high as ~ 60, to see the larger picture. For a shorter pulse than ours, the extent of the saturated regions for all Ω would recede to lower γ, and eventually ranges seen in Fig. 1 are recovered when the pulse duration is shortened to a couple of Rydberg periods. In that case, however, the pulse duration is at the attosecond scale, and even some of the high Ω would then be considered in the field-ionization regime.

As in Fig. 1, the multiphoton ionization peaks are unmistakable and they extend to high values of the Keldysh parameter due to the long pulse duration. The single-photon ionization frequency Ω_1 is again situated at $n/2$, and it is here that the ionization probability is the largest for the widest range of γ. This would be expected from Fig. 1, however one feature that was not clear from Fig. 1 is that the broad region centered at Ω_1 is splitted into sub-peaks for $n = 4$ and 8. We believe that these peaks are due to the energy splitting between the degenerate l-states inside the n-manifolds, and the number of these peaks matching almost one unit of Ω supports this suspicion. As in the rate calculations, multiphoton peaks lead to the single-photon ionization limit, and mark regions of ionization involving multiphoton processes following both direct and indirect paths. Many of these paths result in ionization following an excitation to an excited state, which is evident from the Rydberg series like structure leading up to Ω_1. However, regions in which the ionization happens through a direct multiphoton transition to the continuum, or via an assisted indirect process is not distinguishable from these (γ, Ω)-maps. The slow decaying tail of the ionization probability beyond the single ionization limit Ω_1 is again indicative of the suppression of ionization at high scaled frequencies due to the stabilization seeded by quantum interferences reported in Refs. [12, 13].

The entire (γ, Ω) region seen in Fig. 3 is for $\gamma \gg 1$ as a result of the long laser pulse we had to use to keep the laser duration reasonably long for the entire Ω-range we considered. Here reasonably long means longer than what would be considered an attosecond pulse duration. From the common Keldysh parameter point of view, this is to say that everything seen in Fig. 3 is in the multiphoton regime, and no tunneling takes part in constructing the landscape depicted in Fig. 3. Although Fig. 3 does not distinguish tunneling regions from the multiphoton regions in any way beyond the Keldysh criteria, one may be inclined to assume the Keldysh view-point on account of the multi-photon peaks that appear for $\Omega < n/2$ and extend high up in γ. In order to assess the extent of the multiphoton character in these regions, and to determine if any tunneling contributes to the overall ionization, we look at the momentum distributions of the ionized part of the wave function at various points on the (γ, Ω) landscape seen in Fig. 3.

IV. MOMENTUM DISTRIBUTIONS

In order to evaluate the momentum distribution of the ionized electrons, we follow the same procedure outlined in Ref. [9]. For sake of completes, here we briefly describe the method. In the rate and probability calculations we reported so far, the ionized part of the wave function is removed from the box every time step during the propagation of Eq. 7, in order to prevent unphysical reflections from the radial box edge. This is done using a mask function, which spans 1/3 fo the radial box at the box edge. We retrieve the removed part of the wave function by evaluating

$$\Delta \psi_l(r, t') = [1 - m(r)] \psi_l(r, t') \qquad (9)$$

at every time step, and Fourier transform it to get the momentum space wave function $\Delta \phi(p_\rho, p_z, t')$,

$$\Delta \phi(p_\rho, p_z, t') = 2 \sum_l (-i)^l Y_{l,m}(\theta, \varphi)$$
$$\times \int_0^\infty j_l(pr) \Delta \psi_l(r, t') r^2 \, dr \qquad (10)$$

Here the momentum $p = (p_\rho^2 + p_z^2)^{1/2}$ is in cylindrical coordinates and $j_l(pr)$ are the spherical Bessel functions. We then time propagate $\Delta \phi(p_\rho, p_z, t')$ to a later final time t using the classical action S,

$$\Delta \phi(p_\rho, p_z, t) = \Delta \phi(p_\rho, p_z, t') \, e^{-iS} \qquad (11)$$

For the time-dependent laser field $F(t)$, action S is calculated numerically by integrating p_z^2 along the laser polarization direction

$$S = \frac{1}{2} p_\rho^2 (t - t') + \frac{1}{2} \int_{t'}^t p_z^2 \, dt'' \qquad (12)$$

$$p_z = \int_{t'}^t F(t'') \, dt'' \qquad (13)$$

We are assuming that the ionized electron is freely propagating in the classical laser field in the absence of the Coulomb field of its parent ion, and this method is numerically exact under this assumption.

We pick four points which we consider descriptive of different features seen in Fig. 3. These points are labeled on the (γ, Ω) landscape as A, B, C and D in the top row of Fig. 4. The ordering of the letters are in increasing Ω, whereas no particular relation is implied between the progression of the letters and the Keldysh parameter. Below the (γ, Ω) map for each initial state, the momentum distributions corresponding to the marked points are shown, with the horizontal axis being the momentum component parallel to the laser polarization. In these momentum distributions, momenta corresponding to three different energies are marked with dashed semicircles: (a) energy of the electron when it escapes by absorbing the minimum necessary number of photons from its initial state, (b) the $2U_p$, and (c) the $10U_p$ limits. Classically, the $2U_p$ limit emerges as the drift energy of the electron in the laser field, and marks the maximum energy it can attain when it escapes via the laser field alone without rescattering with its parent ion. The electron can acquire additional energy beyond this limit if rescattering is involved, and there is a relatively flat plateau region in the energy distribution of photoelectrons following $2U_p$, which cuts off around $\sim 10U_p$ [14, 15].

There are a few common physical characteristics seen in all of the momentum maps in Fig. 4. First, ionization by direct photon absorption is manifested as rings in the momentum distributions, with a radius of $p \simeq \sqrt{2(N\omega - I_p)}$ where N is the minimum number of necessary photons required for ionization. This ring is centered at $p = 0$ a.u. if the ionization is directly from the initial state and the electron escapes without rescattering with the ion. However, the center of the ring can be shifted by as much as $\sim 10U_p$ if rescattering occurs [16]. In some cases, the drag in energy caused by the laser field (up to $2U_p$) combined with rescattering can smear the momentum distribution from a well defined circle to a broader ring. On the other hand, tunneling can be recognized as a continuous distribution centered at $p = 0$ a.u., which can extend from $2U_p$ with diminishing amplitude up to $\sim 10U_p$. In the usual context of today's strong field experiments, these would be relatively lower energy electrons when compared with ones appearing at the multiphoton rings when one considers photoionization of noble gas atoms with X-rays in today's modern light sources [17]. Both the multiphoton rings and the tunneling momentum distributions are mostly aligned along the laser polarization direction $(p_\parallel)$, and do not extend as far out in the perpendicular direction. This drop in the electron yield as the observation angle is increased off the laser polarization axis was observed in the angular distributions from photoelectron spectra of Xe [18].

Many of the momentum distributions seen in Fig. 4 display a multiphoton ionization ring at a momentum

corresponding to its lowest order direct multiphoton escape path. However, it is important to keep in mind that these momentum maps are in logarithmic scale, and the contours drop in factors of 2 in the $1s$ distributions, and by factors of 4 in the $4s$ and the $8s$ cases. At points A and B in $1s$, the 3-photon and the 2-photon ionization rings appear sharp in the momentum maps and run almost the entire angular range. In $1s$ (A), the 3-photon rings are centered at $\pm 2U_p$ suggesting that the electron absorbs three photons prior to rescattering from its parent, ion having acquired the $2U_p$ drag from the laser field. The 3-photon rings on the left and the right sides are distinguished in the momentum distribution as the left and the right side back rescattered electrons [16]. The ring in $1s$ (B) however suggests a direct 2-photon ionization, as it is centered at $p = 0$ a.u.. The single photon ring in $1s$ (C) is incomplete, and shows an angular distribution of electrons that mainly come out about the laser polarization axis. On the other hand, the single-photon ionization ring is entirely absent for $1s$ (D), and the momentum distribution is completely contained within the $10U_p$ semicircle. In all these maps for $1s$, even though photoionization rings appear on some of them, they are several factors of 2 lower than the continuous tunneling distributions that appear at the smaller momenta, for the most part contained within the $10U_p$ limit.

Rings of 2-photon ionization are also quite sharp in the momentum distributions for the $4s$ and $8s$ initial states, although they are also substantially smaller than the low energy distribution at small p, suggesting dominance of tunneling at points C for both initial states. However, some photoionization rings are not sharp, but rather dispersed over a momentum range, essentially centered where the ring would normally be found. Particularly, the rings in $8s$ (A) and (D) are most smeared at momenta along the laser polarization direction, and get sharper as the momentum vector becomes more perpendicular to the parallel direction. This is because, it is only the parallel component of the the momentum vector that accumulates energy as the electron is dragged in the laser field, and when the projection of the total momentum vector along this direction is small, there is less dispersion in the momentum distribution. As a result, the rings get broader going down towards the $p_{||}$ axis. Complicated and intricate structures emerge in $4s$ (B) with no particularly prominent structure at the momenta corresponding to 3-photon ionization, and low energy part of the distribution is most prominent. In $4s$ (D), the momentum corresponding to the 5-photon ionization is less than the one corresponding to the $10U_P$ limit, and no particular structure can be made out within the large spread inside the $10U_P$ semicircle. The last interesting feature worth pointing out in these maps is the one seen in $8s$ (B), which are the two circular ridges centered at $p_{||} \simeq \pm 0.03$ a.u.. They clearly have larger radii than the $10U_p$ semicircle, meaning that they correspond to electron distributions which surpass the $10U_p$ limit. These higher energy structures again come from back rescatter-

ing and are much lower in amplitude than the distribution contained within the $10U_P$ limit. These two ridges are perfectly symmetrical in contrast to the asymmetric ridges seen in [16] because in these cases the laser pulse is much longer than what would be considered a few-cycle pulse. They can also clearly be seen in $1s$ (B) and $4s$ (A) in addition to in (C) for all initial states. The common feature in all of the points shown in Fig. 4 is that the momentum distributions are dominated by the low energy electrons − a distinct sign that tunneling dominates despite the high values of the Keldysh parameter.

The points and the corresponding momentum distributions seen in Fig. 4 demonstrate that although the Keldysh parameter is larger than unity, tunneling can still play a prominent role in ionization. The diametric case, in which where $\gamma < 1$, is where tunneling is predicted to dominate the ionization dynamics. To find a contradicting case, we look into the high Ω region for ionization out of the $1s$ state with $\gamma = 0.4$ and $\gamma = 0.8$. For these values of γ there is complete ionization as can be inferred from Fig. 3. For the scaled frequency $\Omega = 8$ beyond the single-photon ionization limit for $1s$ (not seen in Fig. 3), the momentum distributions are seen in Fig. 5. Similar to the momentum maps for $1s$ in Fig. 4, these distributions are also plotted in logarithmic scale with the contours decreasing in factors of 2. The momentum values corresponding to the direct single ionization out of the $1s$ state is again marked with a dashed semicircle, as well as the $2U_p$ and the $10U_p$ limits as before. At the lower Keldysh parameter 0.4, the single-photon momentum is between the $2U_p$ and the $10U_p$ limits, whereas it is larger than the $10U_p$ momentum for $\gamma = 0.8$. In either case, there is nothing with momentum less than the $2U_p$ momentum limit, suggesting that the broadly spread semicircular ridges straddling the single-photon momenta are indeed the momentum ridges from the single-photon ionization. This is most clear at the lower intensity of $\gamma = 0.8$, where the single-photon ridge is much more sharper at the expected momentum. In this case there is nothing before the $10U_p$ limit, and the ridge seen is entirely due to single-photon ionization. The same is also true for the $\gamma = 0.4$ case, however lower γ means higher field strength resulting in the dispersion of the sharper peak seen at the lower field of $\gamma = 0.8$. This demonstrates that although $\gamma < 1$, we can find regions in the (γ, Ω) space where the usual Keldysh ansatz does not hold.

V. SUMMARY

In conclusion, we have presented photo-ionization rates and probabilities out of the $1s$, $4s$, $8s$ and $16s$ states of Hydrogen atom for wide ranges of the Keldysh parameter γ and the scaled frequency Ω. We map the ionization rates for a continuous wave (cw) laser and probabilities for a laser pulse with a fixed duration in units of the classical orbital period in (γ, Ω) space. Taking constant field

strength and constant frequency slices from the (γ, Ω) map, well known hallmarks and structures can be reconstructed from both the common strong field standpoint (Γ versus F) and the spectroscopic standpoint (Γ versus Ω) for ionization rates, such as multiphoton resonances, exponential decay and frequency independent, both characteristics of tunneling decay [2, 7]. Suppression of ionization can also be seen beyond the single-photon ionization limit $\Omega_1 = n/2$ in both (γ, Ω) maps for the rate and the probability, which was reported in Refs. [12, 13].

We further show that ionization regions dominated by the field-ionization and multiphoton processes may both exist in the high Keldysh parameter region $\gamma > 1$ by calculating the momentum distributions for the ionized electrons at particular points on the (γ, Ω) landscape. We find that although the Keldysh ansatz suggests a predominantly multiphoton picture for ionization in all of Fig. 3 due to its large γ range, below the single-photon ionization limit Ω_1 both tunneling and multiphoton processes contribute to ionization with tunneling leading to most of the ionization. Tunneling predicted by the low Keldysh parameter is also absent at $\gamma = 0.4$ and 0.8 above the Ω_1 limit for ionization out of the ground state, as seen from the momentum distributions shown in Fig. 5. In this case, ionization is entirely due to single photon absorption with a sharper momentum ring for the higher γ (lower intensity), and with a more dispersed ring for the lower γ (higher intensity).

The coupling of the scaled frequency with the Keldysh parameter in this sense serves to compliment γ for its inadequacy to account for the relevance of the time scale inherently present in the bound electron dynamics, i.e. the Rydberg period of the electron, as Keldysh-like theories assume no dynamics for the electron inside the potential well prior to ionization. The dynamical characterization outlined by γ is further augmented by inclusion of the scaled frequency in this picture, because the tunneling-multiphoton dichotomy suggested by the Keldysh parameter does not observe conservation of energy since it comes about within a strictly tunneling scenario. Both dynamical regimes of ionization can be attained for a chosen small value of γ, by varying the scaled frequency, and for the most part, they coexist in vast regions on the (γ, Ω) map.

VI. ACKNOWLEDGMENTS

[1] V. S. Popov, Physics Uspekhi **47**, 855 (2004).

[2] N. B. Delone and V. P. Krainov, Physics-Uspekhi **41**, 469 (1998).

[3] L. V. Keldysh, Zh. Eksp. Theor. Fiz. **47**, 1945 (1964) [Sov. Phys. JETP **20**, 1307 (1965)].

[4] H. R. Reiss, Prog. Quant. Electr. **16**, 1 (1992).

[5] P. W. Milonni, Phys. Rev. A **38**, 2682 (1988).

[6] F. Trombetta, S. Basile, and G. Ferrante, Phys. Rev. A **40**, 2774 (1989).

[7] M. Dörr, R. M. Potvliege, D. Proulx, and R. Shakeshaft, Phys. Rev. A **42**, 4138 (1990).

[8] H. R. Reiss, Phys. Rev. A **82**, 023418 (2010).

[9] Y. Ni, S. Zamith, F. Lepine, T. Martchenko, M Kling, O. Ghafur, H. G. Muller, G. Berden, F. Robicheaux, and M. J. J. Vrakking, Phys. Rev. A **78**, 013413 (2008).

[10] J. H. Gurian, K. R. Overstreet, H. Maeda, and T. F. Gallagher, Phys. Rev. A **82**, 043415 (2010).

[11] T. Topcu and F. Robicheaux, J. Phys. B **40**, 1925 (2007).

[12] E. J. Galvez, B. E. Sauer, L. Moorman, P. M. Koch, and D. Richards, Phys. Rev. Lett. **61**, 2011 (1988).

[13] H. Maeda and T. F. Gallagher, Phys. Rev. Lett. **93**, 193002 (2004).

[14] P. B. Corkum, N. H. Burnett, and F. Brunel, Phys. Rev. Lett. **62**, 1259 (1989).

[15] B. Walker, B. Sheehy, K. C. Kulander, and L. F. Di-Mauro, Phys. Rev. Lett. **77**, 5031 (1996).

[16] Z. Chen, T. Morishita, A.-T. Le, and C. D. Lin, Phys. Rev. A **76**, 043402 (2007).

[17] N. Berrah, J. Bozek, J. T. Costello, S. Düsterer, L. Fang, J. Feldhaus, H. Fukuzawa, M. Hoener, Y. H. Jiang, P. Johnsson, E. T. Kennedy, M. Meyer, R. Moshammer, P. Radcliffe, M. Richter, A. Rouzèe, A. Rudenko, A. A. Sorokin, K. Tiedtke, K. Ueda, J. Ullrich, amd M. J. J. Vrakking, Journal of Modern Optics **57**, 1015 (2010).

[18] M. Okunishi, T. Morishita, G. Prümper, K. Shimada, C. D. Lin, and K, Ueda, Phys. Rev. Lett. **100**, 143001 (2008).

Fig. 01

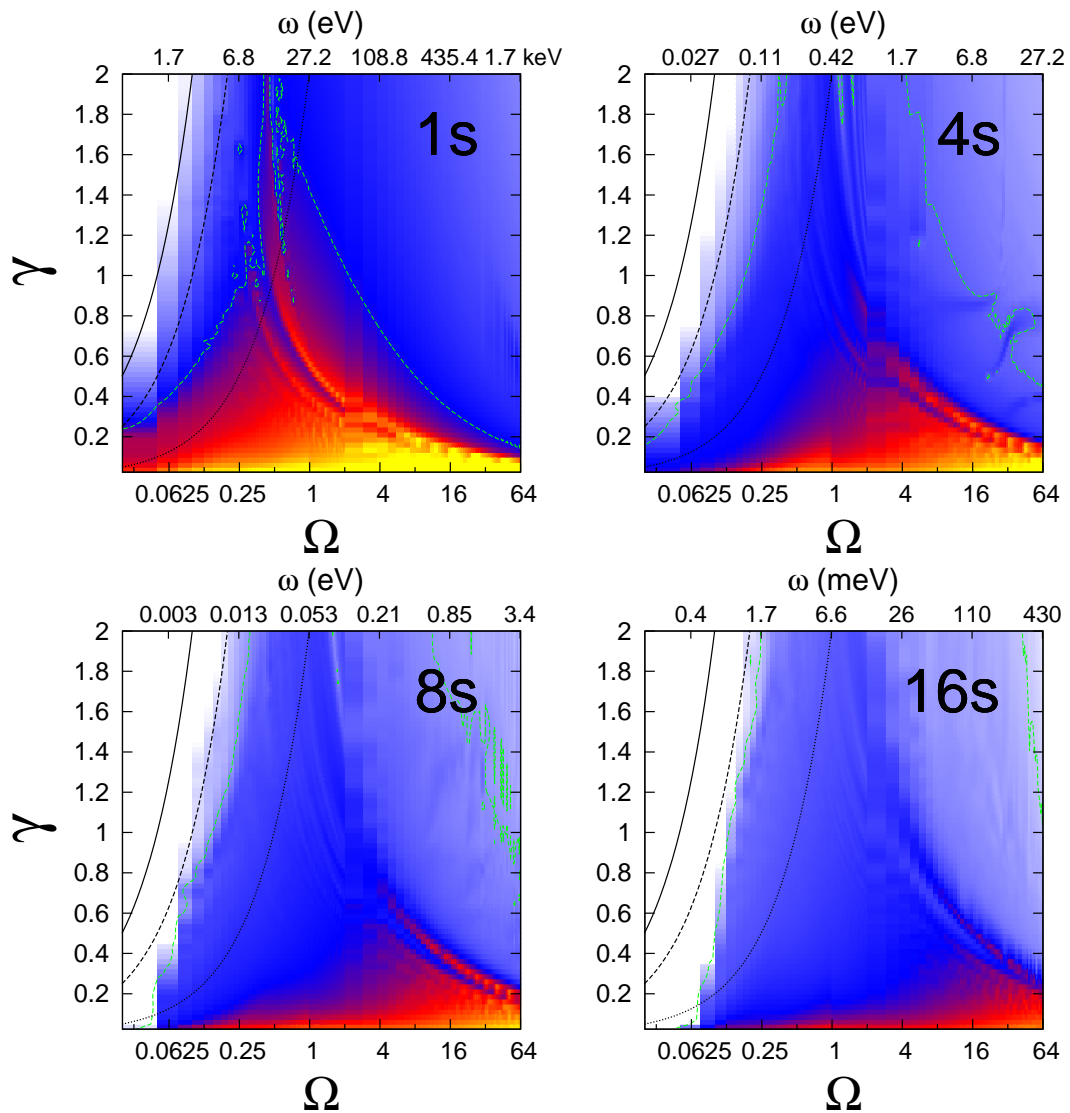
FIG. 1: (Color online) Keldysh parameter γ versus scaled frequency Ω for $n = 1$, 4, 8 and 16 with the atomic wave packet launched as an s-wave. Along the solid, dashed, and dotted lines $F = 0.05$, 0.1, and 0.5 a.u. from left to right, where F is the peak electric field strength. The Ω-axes are in $\log_2$ scale whereas the γ-axes are in linear scale. The ionization rates Γ are plotted in $\log_{10}$ scale with the brightest yellow being 2 a.u. and the faintest blue being -4.5 a.u.
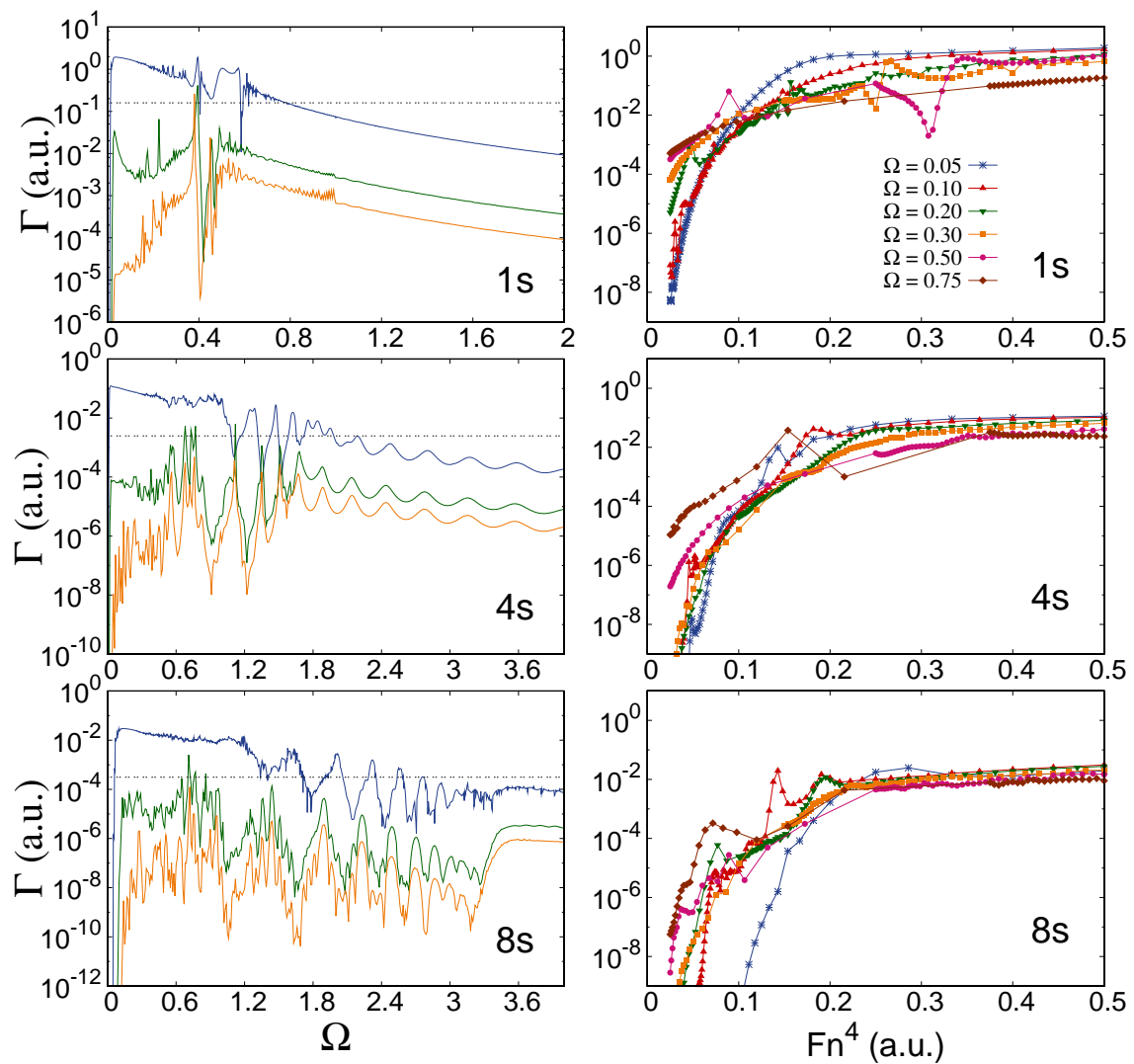
FIG. 2: (Color online) (Left column) Ionization rates Γ as a function of the scaled frequency Ω out of $n = 1s$, $4s$ and $8s$ states of Hydrogen for three different peak field strengths: $F = 0.05$, 0.1, and 0.5 a.u. from top to bottom. These corresond to intensities of 1.8×10^{17}, 3.6×10^{15}, and 1.8×10^{15} W/cm^2. The Γ axes are in $\log_{10}$ scale. (Right column) Γ as a function of the scaled peak electric field strength Fn^4 for several Ω for ionization out of the same states. Again, the Γ axes are plotted in $\log_{10}$ scale.
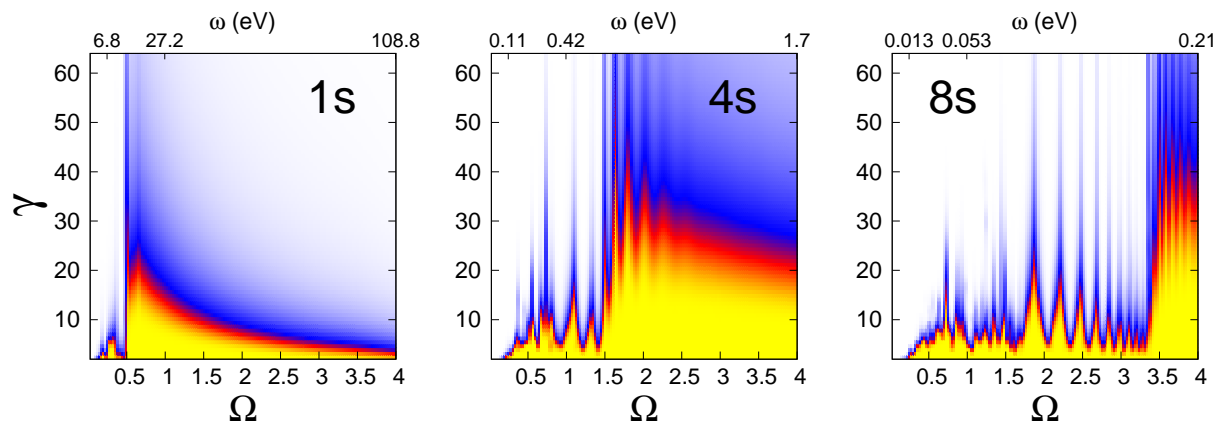
Fig. 03

FIG. 3: (Color online) Quantum ionization probabilities for ionization out of $1s$, $4s$, and $8s$ states of Hydrogen for a laser pulse with a width of 160 Rydberg periods at FWHM. Both Ω and γ axes are in linear scale and the ionization probabilities are in log_{10} scale. The yellow regions indicate complete ionization and the multiphoton ionization peaks as well as the suppression at high scaled frequencies are clearly visible.
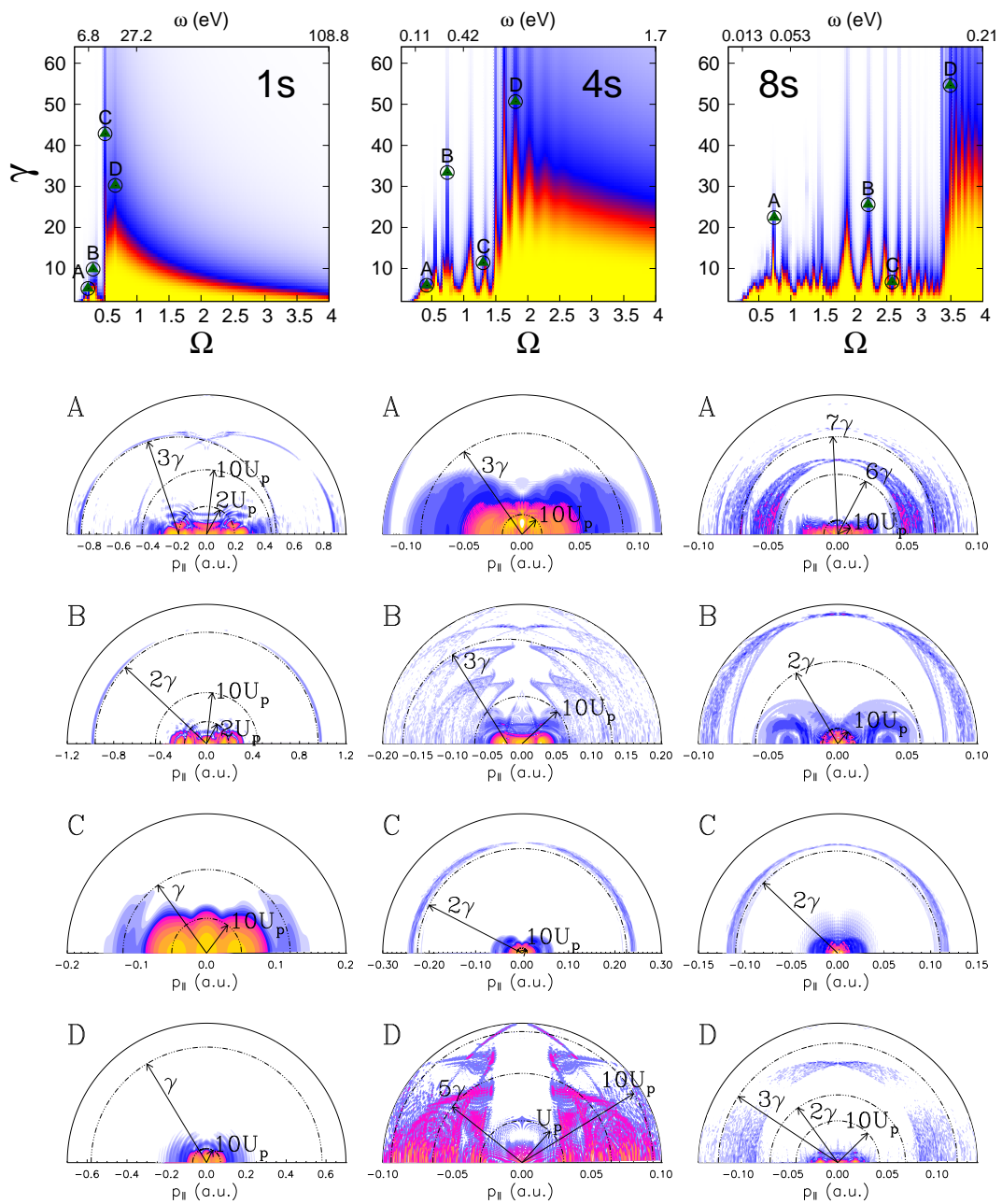
FIG. 4: (Color online) Momentum maps for the $\gamma > 1$ region for selected points from the ionization probability landscape of Fig. 3. The momentum distributions have only the momentum component parallel to the laser polarization marked as the horizontal axis and the perpendicular axis is implied from the cylindrical symmetry of the problem. Dashed semicircles mark momenta values corresponding to lowest order multiphoton ionization from initial state, the $2U_p$, and the $10U_p$ limits. They are plotted in logarithmic scale to bring out both multiphoton and tunneling features on the same plot.
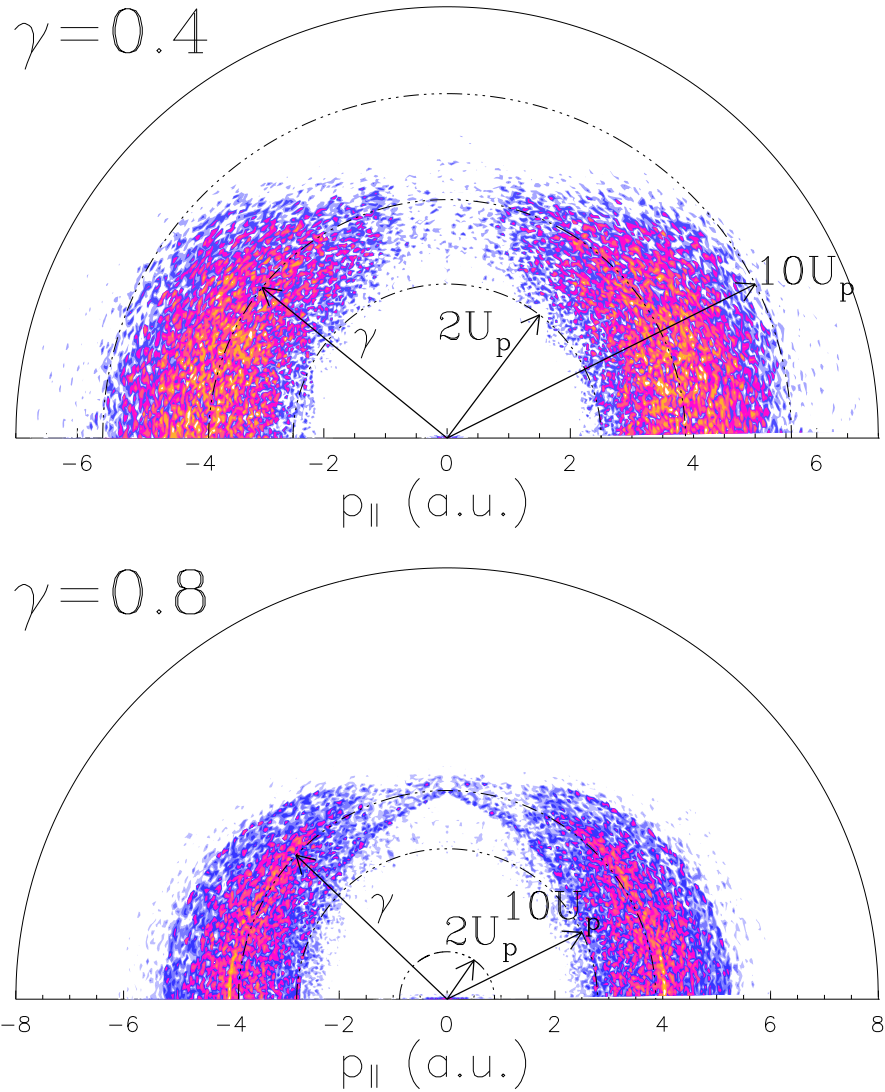
Fig. 05

FIG. 5: (Color online) Momentum distributions for low Keldysh parameters $\gamma = 0.4$ and $\gamma = 0.8$. Both distributions are for ionization out of the $1s$ initial state with $\Omega = 8$ in the single-photon ionization regime. Semicircles again mark the single-photon ionization momentum values, as well as the $2U_p$ and the $10U_p$ limits.